Experiments in Fluids (2018) 59:167
https://doi.org/10.1007/s00348-018-2618-9

RESEARCH ARTICLE

Dual fluorescence ratiometric technique for micromixing characterization

David C. Bedding[1] · **Carlos H. Hidrovo**[1]

Received: 27 March 2018 / Revised: 20 September 2018 / Accepted: 22 September 2018

Abstract

To probe high-speed mixing within microfluidic devices, an imaging technique that uses fluorescent emissions as an indicator of fluorophore concentration has been developed. Given that fluorescent emission varies linearly with excitation intensity, higher powered excitation sources, such as lasers, must be used to collect sufficient emission information over short periods of time. However, since laser-based excitation sources tend to be spatially and temporally non-homogeneous, a ratiometric imaging technique is used to correct these fluctuations without removing concentration information. Image processing is used to determine the homogeneity of the ratio values and, by correlation to the concentration, the level of mixing for the whole sample can be determined. The accuracy of this technique is assessed by comparing experimental results to a parallel flow micromixer COMSOL simulation of the actual concentration and overlaying imaging results. The dual fluorescence ratiometric technique is accurate within 11% of the simulations. The technique is then used to characterize a serpentine droplet micromixer which uses chaotic advection to increase the rate of mixing throughout the sample. This system is characterized using four different oil flow rates for mixing measurements taken for three different height locations throughout the channel.

✉ Carlos H. Hidrovo
hidrovo@neu.edu

David C. Bedding
bedding.d@husky.neu.edu

[1] Multiscale Thermal Fluids Laboratory, Northeastern University, Boston, MA, USA

Published online: 13 October 2018

Graphical abstract

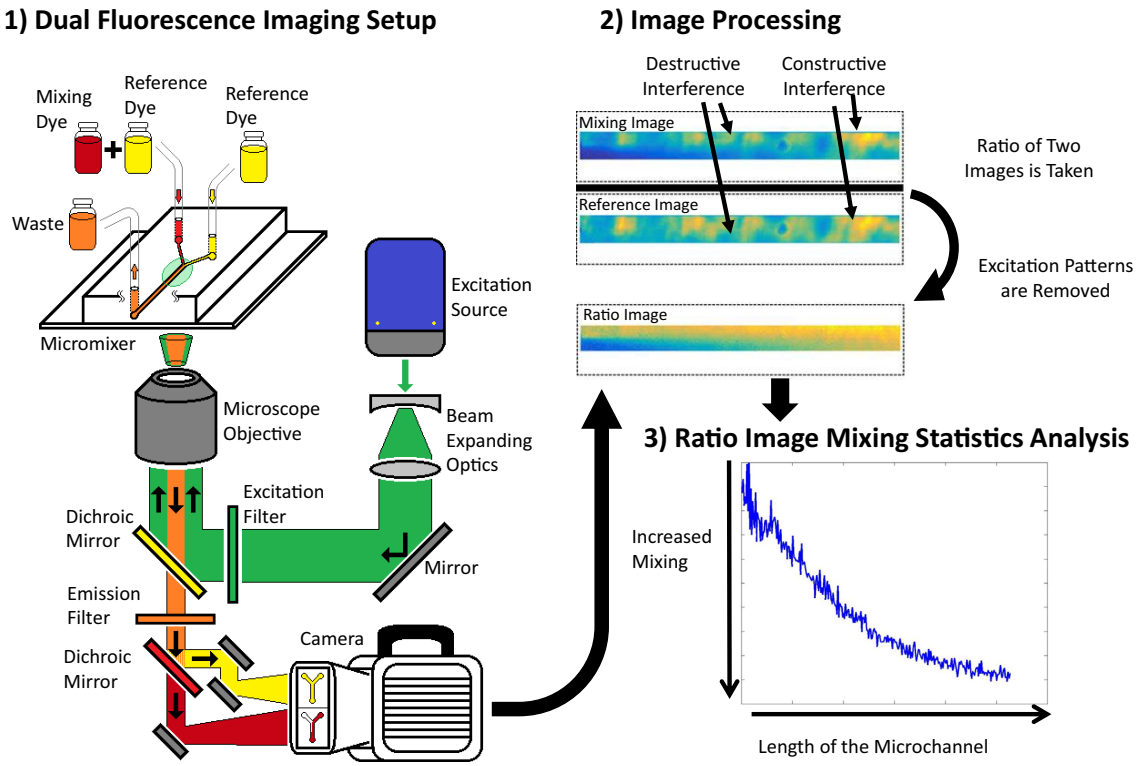

1 Introduction

A technique that utilizes high-speed imaging in conjunction with a high-power excitation source was developed to probe fast mixing within microfluidic systems. This technique uses fluorescent emissions as an expression of molecular concentration to determine homogeneity throughout the sample. Fluorescent indicators are most commonly used for detection within biological samples, specifically for genetic precursors (Waggoner 2006; Huebner et al. 2007), or protein analysis (Schwille 2005; Wang et al. 2005; Dittrich and Manz 2006; Huebner et al. 2009), but fluorescent information can also be used for quantitative measurements and the extraction of accurate, nuanced information. One such use of this information is for the development and increased understanding of mixing phenomena within microfluidic systems.

Microfluidic mixing is hampered due to inherently low Reynolds number, leading to mixing that is slow and diffusion-based. As a result many different micromixers must use complex active (Yang et al. 2001; Abbas et al. 2013) and passive components (Lin et al. 2004; Wu and Nguyen 2005), to promote these behaviors. Since many of these micromixers incorporate complex physics, several techniques have been developed to determine the homogeneity of these samples and the effectiveness of these micromixers. Many of these techniques are either intrusive or have relatively low signal and are thus unsuited for transient measurements, such as Spontaneous Raman Scattering (Mayinger et al. 2010). To probe faster systems techniques such as Laser-Induced Fluorescence (LIF) can be utilized in conjunction with a high-speed camera to collect large quantities of emission information at high frequencies.

The process of taking optical measurements involves using a camera to collect fluorescent dye emissions for discrete areas and values in the form of pixels. The fluorophore-emission process is characterized by three steps: excitation, excited state lifetime, and emission. Fluorescent emission output is a function of dye properties, concentration, sample thickness, and excitation intensity. Among these parameters, excitation intensity is the only one that acts as a semi-random scalar field on recorded images.

A method for correcting this kind of excitation-based information is ratiometric imaging, where fluorophore emissions of two dyes within a sample are decomposed into their constituent wavelengths, isolating the emissions of dyes, and a ratio of these two images is taken

(Coppeta and Rogers 1998). Isolation of these dye emissions is achieved through the incorporation of optical filters and dichroic mirrors, a method found in (Sakakibara and Adrian 1999). The ratiometric image is constructed by dividing the intensity distributions in one image by the intensity distribution in the other image, thus eliminating linear scalars acting on both images (Hidrovo and Hart 2001). Ratiometric images have been used to remove excitation for previous microfluidic applications. Ratiometric images have been used to take thermal measurements throughout a microchannel (Natrajan and Christensen 2009; Christensen and Natrajan 2010; Kim and Yoda 2010; Kim et al. 2015). These systems take ratios of temperature sensitive dye emissions to a non-temperature sensitive dye emission, and a temperature calibration can be established. Ratiometric imaging has also been used for film thickness measurements in (Hidrovo and Hart 2001), where absorption and remission between the two dyes changes the ratio of the emission per unit thickness, allowing for instantaneous 2D mapping of film thickness. In the vein of microfluidic mixers, ratiometric imaging has also been used to analyze laminar flow micromixers. Micromixers exhibit continuous changes in concentration throughout the sample, which are indistinguishable from excitation patterns when using a single fluorescence system. Works like (Kise et al. 2014) remove the dependence on absorbance on concentration, through the use of a ratio of absorbance values at different wavenumbers.

In this paper, we compare mixing statistics calculated from dual-fluorescence ratiometric images to those calculated from single-fluorescence images. In addition to this, two different excitation sources are compared; a continuous emission laser, and a white light emission source, and two different cameras are utilized; a CCD with higher spatial resolution and a large dynamic range, and a lower resolution CMOS. This technique is characterized using a lower speed diffusion-based micromixer similar to those found in (Yamada et al. 2004; Shi et al. 2012; Gashti et al. 2016), and then applied to a higher speed micromixer that induces chaotic advection to promote stirring and increase the rate of mixing within a sample (Hassan 1984; Baroud 2010). A depiction of these two micromixer designs can be found in Fig. 1. Although chaotic advection can be utilized in stream micromixers (Jones et al. 1989; Liu et al. 2000), droplet microfluidic systems are increasingly more prevalent due to their ability to produce uniform confined volumes at high speeds (Baroud et al. 2010; Tirandazi and Hidrovo 2017) for processes such as digital droplet PCR (Baker 2012; Pav et al. 2016). These droplet microfluidic systems are physically complex and are computationally difficult to simulate, which is why they were selected to prove the versatility of our technique.

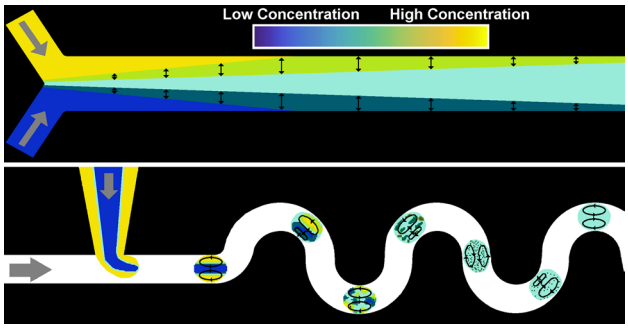

Fig. 1 Example of the two different micromixers that are used in experimentation, a laminar stream micromixer (top) and a droplet micromixer (bottom). Black arrows denote the process of diffusion (top) or advection (bottom), while gray arrows represent fluids being pumped into the system

2 Methods

2.1 Imaging technique: fluorescence

The fundamental principle behind our spatial-intensity mixing diagnostic is fluorescent emission. This internal process consists of the electrons being raised to a higher energy state through exposure to the incoming photon. After being raised to the higher energy state, these electrons will then return to the original lower energy state, releasing a photon of a higher wavelength in the process. The amount of energy in the released photon is determined based on the molar absorption coefficient of that given fluorophore. The molar absorption coefficient of a dye, alongside its concentration leads to an exponential decay of the excitation intensity known as the Lambert–Beer's law:

$$\frac{I_{\mathrm{Ex},x}}{I_{\mathrm{Ex},0}} = \exp\left(-\varepsilon C x\right), \tag{1}$$

where εC is the combined molar absorption coefficient times concentration product of all the fluorophores within the control volume, x is the finite distance the excitation light has travelled through the control volume, $I_{\mathrm{Ex},x}$ is the excitation intensity at depth x, and $\mathrm{I}_{\mathrm{Ex},0}$ is the excitation intensity at the surface ($x=0$). Integration of the Lambert–Beer law over a finite thickness L leads to the following equation for the fluorescence emission of a specific fluorophore:

$$I_{\mathrm{Em}\,i} = I_{\mathrm{Ex},0}\frac{\varepsilon_i\left(\lambda_{\mathrm{filt}\,i}\right)C_i\Phi_i[1-\exp(-\varepsilon(\lambda_{\mathrm{Ex}})Cx)]}{\varepsilon(\lambda_{\mathrm{Ex}})C}, \tag{2}$$

where ε_i is the molar absorption coefficient of the fluorophore in question, and C_i its concentration. The full

derivation can be found in (Hidrovo and Hart 2001). This equation also includes the quantum efficiency of the flurophore, Φ_i, which is the ratio of the emitted energy to absorbed energy by the fluorophore.

2.2 Imaging technique: ratiometric imaging

To eliminate the excitation intensities within a discrete sample set, a ratiometric technique is implemented to remove all non-concentration-based information within the sample as described in (Christensen and Natrajan 2010). To utilize this ratiometric imaging technique, two different images for identical spatial and temporal coordinates must be taken. These two images are distinguished from one-another by seeding the microfluidic sample with two fluorescent dyes with distinct emission spectrums. Since these dyes have substantially different emission spectrums, images containing both of these emission can be decomposed on the basis of their constituent wavelengths, isolating the dye emissions into their own respective images. The ratio of these decomposed emissions is given by:

$$R_{\mathrm{Em}} = \frac{I_{\mathrm{Em1}}}{I_{\mathrm{Em2}}}, \tag{3}$$

where the subscripts 1 and 2 denote the emission intensity of the emission fields generated by splitting the image. The numerator in the ratiometric equation consists of emissions from a fluorophore seeded evenly throughout one of the two mixing fluids, acting as an indicator of the level of mixing throughout the sample. The denominator shows emissions of a second fluorophore seeded evenly throughout both mixing fluids, acting as a canvas for the excitation pattern.

Since both of the emissions are functions of the characteristics of the fluorescent dyes, the ratio of the two emissions can be written as:

$$R(x,y) = \frac{I_{\mathrm{Em1}}}{I_{\mathrm{Em2}}} = \frac{I_{\mathrm{Ex},0}\frac{\varepsilon_1(\lambda_{\mathrm{filt1}})C_1\Phi_1[1-\exp(-\varepsilon(\lambda_{\mathrm{Ex}})CL)]}{\varepsilon(\lambda_{\mathrm{Ex}})C}}{I_{\mathrm{Ex},0}\frac{\varepsilon_2(\lambda_{\mathrm{filt2}})C_2\Phi_2[1-\exp(-\varepsilon(\lambda_{\mathrm{Ex}})CL)]}{\varepsilon(\lambda_{\mathrm{Ex}})C}}. \tag{4}$$

where the excitation intensities are eliminated, resulting in:

$$R(x,y) = \frac{I_{\mathrm{Em1}}}{I_{\mathrm{Em2}}} = \frac{\varepsilon_1(\lambda_{\mathrm{filt1}})C_1\Phi_1[1-\exp(-\varepsilon(\lambda_{\mathrm{Ex}})CL)]}{\varepsilon_2(\lambda_{\mathrm{filt2}})C_2\Phi_2[1-\exp(-\varepsilon(\lambda_{\mathrm{Ex}})CL)]}. \tag{5}$$

Since most microfluidic systems are of constant thickness, the only impactful terms are the quantum efficiency, absorption coefficient, and the molecular concentration. The process of ratiometric imaging can be shown in Fig. 2, where a concentration gradient with an overlaid excitation profile was divided by a uniform concentration profile with the same overlaid non-uniform laser excitation profile, resulting in a ratiometric image on the right.

In addition, all emissions are scaled by a "monitoring efficiency" (Wang et al. 1988), which is the fraction of the total fluorescent emission that can be collected by the sensor. Since this is a constant scalar over the entire image, the monitoring efficiency does not change mixing statistics in both ratiometric and non-ratiometric imaging. As a result the monitoring efficiency is ignored for our purposes.

2.3 Mixing statistics

Collected ratio values are recorded as scalar fields, which can then be utilized to understand the mass convective-diffusive interactions over time. For the purposes of this paper, mixing is calculated by measuring the amount of solute diffusion that has occurred throughout the sample. While some previous works have measured striations and gradients throughout a sample (Lin et al. 2004; Carroll and Hidrovo 2012), these are just indicators that show the potential for future diffusion.

The level of mixing within a system is determined by calculating the standard deviation of the concentration values within the sample, as done in (Carroll and Hidrovo 2012) and (Kling and Mewes 2004), using the equation:

$$\sigma = \left[\frac{\int_A \left(C-\mu_C\right)^2 \mathrm{d}A}{A}\right]^{1/2}, \tag{6}$$

where μ_C is the average concentration throughout the entire sample, defined as:

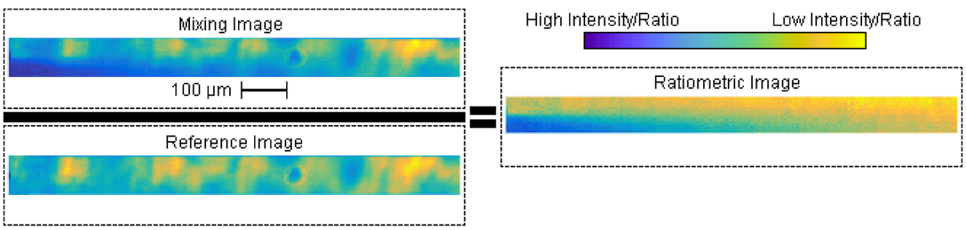

Fig. 2 Ratiometric imaging technique shown using pseudo-colored image. The mixing image (shorter wavelength emissions) is in the top left, while the reference image (longer wavelength emissions) is in the bottom left. The ratio of these two images can be seen on the right

$$\mu_C = \frac{\int_A C \, dA}{A}, \tag{7}$$

increased standard deviation corresponds to less homogeneity throughout the sample, and thus a lower level of mixing, and vice versa. Combining these equations with the total fluorescent emission output (1) results in:

$$\sigma = \left[\frac{\int_A \left(I_{\mathrm{Em}} - \mu_{\mathrm{Em}} \right)^2 dA}{A} \right]^{1/2}, \tag{8}$$

since intensity emissions for a sample are recorded as discrete pixels, these relations can be converted to:

$$\sigma = \left[\frac{\sum_{i=1}^{N} \left(I_{\mathrm{Em}} - \mu_{\mathrm{Em}} \right)^2}{N-1} \right]^{1/2} \quad \text{and} \quad \mu_C = \frac{\sum_{i=1}^{N} I_{\mathrm{Em}}}{N}, \tag{9}$$

or,

$$\sigma = \left[\frac{\sum_{i=1}^{N} \left(R_{\mathrm{Em}} - \mu_{\mathrm{Em}} \right)^2}{N-1} \right]^{1/2} \quad \text{and} \quad \mu_C = \frac{\sum_{i=1}^{N} R_{\mathrm{Em}}}{N}, \tag{10}$$

for ratiometric imaging. Though this equation both exhibits the appropriate trends, as well as establishes a completely mixed condition, it does not accurately convey the intermediary levels of mixing at a given location. This is due to the standard deviation being tied to the magnitude of the emission term. Compare two unmixed cases; one consisting of emissions: $I_{\mathrm{Em}} = 0$ and $I_{\mathrm{Em}} = 100$, and one consisting of emissions: $I_{\mathrm{Em}} = 0$ and $I_{\mathrm{Em}} = 50$. Both of these cases are completely unmixed, yet the former exhibits a higher standard deviation. To correct for this, the normalized standard deviation is used:

$$\sigma_n = \frac{\sigma}{\mu} = \left[\frac{\sum_{i=1}^{N} \left(\frac{R}{\mu} - 1 \right)^2}{N-1} \right]^{1/2}, \tag{11}$$

which establishes both fully unmixed and fully mixed conditions for the discrete scalar fields.

2.4 Experimental setup

The goal of this work is to verify the effectiveness of our imaging technique in determining the level of mixing throughout a sample, and then characterize a more complex micromixer to prove the effectiveness of the technique. The two microfluidic systems used for these purposes are a laminar two-stream micromixer, and a two-phase droplet micromixer. Micromixers are created using a process of photolithography followed by soft lithography. Through the process of photolithography microchannel geometry is imprinted as negatives on silicon wafers. A thick layer of polydimethylsiloxane (PDMS) substrate is poured over these channel negatives, hardened, and then peeled off. Fluid inlets and outlets are created using biopsy punches (125 μm, Albert). These microfluidic devices are then oxygen-plasma cleaned (Harrick Plasma, PDC-32G-2) and bonded to a silicon-glass microscope slide.

Two geometries were used to determine mixing diagnostics within the samples, a laminar stream micromixer, and a droplet micromixer. The laminar stream micromixer consists of two rectangular channels with a 50×50 μm^2 cross-section meeting at a 120° intersection before merging into a 100×50 μm^2 channel. The droplet mixing system consists of three microfluidic channels merging together and leading perpendicularly into a larger main channel containing a continuous flow of oil. The main channel follows a serpentine path, promoting chaotic advection and internal fluid redistribution. The main serpentine channel is a square cross-section of 50×50 μm^2 and the disperse phase site is 50×50 μm^2 wide at its narrowest point, where it is flush with the serpentine channel wall.

Fluid injection is implemented using syringes (Hamilton Company) in conjunction with syringe pumps (Harvard Apparatus). For the laminar stream cases, mixing fluids are injected at flow rates of 5 μL/hr. The droplet microfluidic system injects mixing and reference dye solutions at a total rate of 8 μL/min, while the disperse phase is injected at a variety of flow rates ranging from 4 μL/min to 13 μL/min.

To implement a proper ratiometric imaging technique, the working fluid is seeded with two fluorescent dyes, a mixing dye and a reference dye. These dyes must have absorption spectrums that overlap with the illumination source, but vary significantly in their emission spectrums (Natrajan and Christensen 2009). With these constraints in place, Sulforhodamine G (Sigma Aldrich) and Sulforhodamine 640 (Exciton) were selected as the mixing dye and reference dye, respectively (Coppeta and Rogers 1998).

The optical rig consists of an illumination source; either a continuous-wave laser (532 nm Q-Switched Laser, Changchun New Industries), or a white-light source (Lumen 200, Prior Scientific), and a series of beam expanding and collimating optics to ensure a sufficiently wide illumination profile. The excitation then passes through a dichroic mirror cube (Chroma, ZT532rdc) consisting of an excitation filter, a dichroic mirror, and an emission filter. The excitation filter (Chroma, ZET532/10X) is used to prevent spurious emissions from being directly imprinted onto the camera sensor. The dichroic mirror transmits all wavelengths shorter than 545 nm while

reflecting higher wavelengths. Thus, low wavelength excitations pass through the dichroic, fill the objective (Nikon 5×), and illuminate the sample. Fluorescent dye within the sample absorbs the excitation source and exhibits a Stoke's Shift, emitting higher wavelength photons that pass back through the objective and through the dichroic mirror toward the imaging capturing module.

For single-dye LIF the dye's emission is recorded directly to the camera sensor, while for double-dye LIF the emissions pass through an optical beamsplitter (Photometrics, DV2) before reaching the sensor. The beamsplitter uses an additional dichroic mirror (Photometrics, ZT561) to separate the emissions of the two dyes and display the results side-by-side on the camera sensor. These split signals are run through additional filters; the lower wavelength emissions through a 537 ± 29 nm filter, and the higher wavelength emission through the 600 nm longpass filter (Thorlabs) to further isolate the emissions. The fluorescent absorption and emission spectrums for the selected dyes with overlays of the filtered viewing sections can be found in Fig. 3.

Overlap between the emission spectrum of one dye and the absorption spectrum of another dye results in a phenomenon called reabsorption. Reabsorption has two effects that must be taken into account when dealing with a system of two dyes: (1) boosting of the emission of the dye doing the reabsorption, and (2) decrease of the emission of the dye being reabsorbed. Since the intensity of dye emissions are much lower than that of the laser excitation, the boosting effect can be safely neglected in our formulations. Intensity loses due to reabsorption are, however, significant. Incorporating this emission reduction for the reabsorbed emission, our ratiometric ratio equation (Eq. 5) becomes:

$$R = \frac{\varepsilon_1\left(\lambda_{\text{filt1}}\right) C_1 \Phi_1 \frac{\left[1-\exp\left(-\left\{\varepsilon\left(\lambda_{\text{Ex}}\right)C+\varepsilon_2\left(\lambda_{\text{filt1}}\right)C_2\right\}L\right)\right]}{\varepsilon\left(\lambda_{Ex}\right)C+\varepsilon_2\left(\lambda_{\text{filt1}}\right)C_2}}{\varepsilon_2\left(\lambda_{\text{filt2}}\right) C_2 \Phi_2 \frac{\left[1-\exp\left(-\varepsilon\left(\lambda_{Ex}\right)CL\right)\right]}{\varepsilon\left(\lambda_{Ex}\right)C}}. \tag{12}$$

Two cameras were used during experimentation; a charge-couple device (CCD) and a higher-speed complementary metal oxide semiconductor (CMOS) camera. The CCD camera (Coolsnap HQ) allows for more accurate spatial measurements, utilizing smaller 6.45×6.45-μm pixels and a more accurate interline sensor. In comparison, the CMOS camera (Fastcam SA5) allows for more accurate transient measurements but makes sacrifices such as larger 20×20 μm pixels and increasing sensor noise. For laminar stream mixing cases, the CCD is used to determine the effectiveness of the technique, while for high-speed droplet mixing a CMOS allows many more measurements, allowing for a much deeper understanding of the transient.

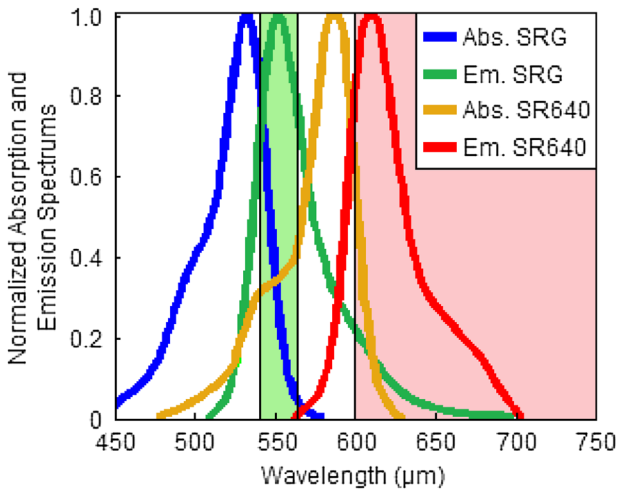

Fig. 3 Absorption and emission spectrums for sulforhodamine G and sulforhodamine 640. Regions highlighted in green and red represent the wavelengths visible after the raw data was split by the Dual-View filter

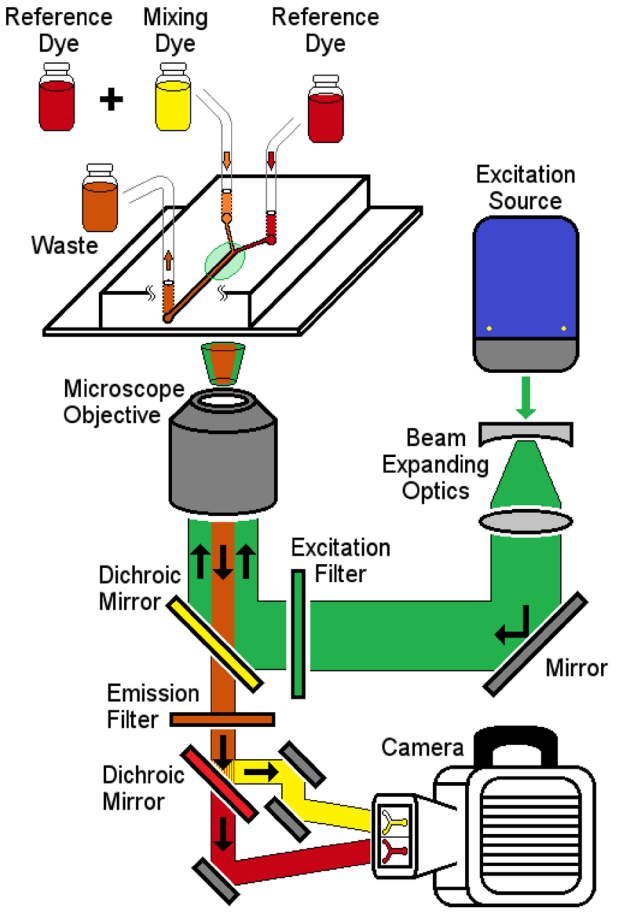

Fig. 4 Experimental set up used for collecting fluorescent emission information from a micromixer

Images recorded by both cameras are 12-bit grayscale images, allowing for up to 4096 levels for each pixel. A complete schematic of the optical setup can be found in Fig. 4. Raw images consist of two images located side-by-side, which are mechanically aligned so that the two images are spatially similar. As mechanical alignment cannot is not sufficient to achieve perfect alignment between the two images, a particle image velocimetry (PIV) correlation is used to achieve sub-pixel accuracy in the alignment. This is achieved by imaging a highly patterned surface, such as sandpaper, and performing statistical correlations between pixels in both images. These correlations are recorded as displacement vectors, and pixels are shifted in one image to properly the other. The process of a subpixel shift is shown in Fig. 5. A full description of this process can be found in (Soloff and Al 1997), and a similar experimental setup using a dichroic filter to split the emission can be found in (Sakakibara and Adrian 2004; Kim et al. 2015) and has previously been used to analyze micromixers like in (Kling and Mewes 2003).

3 Results

3.1 Laminar mixer: simulation

To verify our imaging technique, a simple two stream transport simulation was conducted using COMSOL Multiphysics. This simulation consists of two identical inlet channels that come together at a 120°, these inlet channels are 60 µm wide and 50 µm tall, and the flow inside exhibits Poiseuille flow. One of the inlet streams contains a 0.25 mg/mL dye concentration, while the other stream is contains pure liquid water. The solute seeded within the sample exhibits a diffusion coefficient equal to that of the mixing dye, Sulforhodamine G, of 2.5×10^{-10} $m^2 s^{-1}$ (Jia et al. 2012). The two inlets merge and then form a main channel with a width of 120 µm.

Given the deformable nature of PDMS microchannels, a change in channel thickness due to pressure gradient must be taken into account. An analysis conducted in (Hardy et al. 2009) developed a relationship between constant volume flow rate and a change of height in a PDMS microchannel. Applying a worst-case scenario, in terms of PDMS material properties, shows that the maximum microchannel thickness is 50.0356 µm tall at the vertex of the Y-junction. Given that this is a negligible 0.07% change in overall thickness, it was deemed appropriate to use static walls in the simulation.

The mixing statistic (Eq. 11) is calculated for each cross-section giving a mixing values for discrete areas down the length of the main channel. Statistics for simulations and experiments are taken at the mid-plane, though the variations in concentration at different heights throughout the sample are largely insignificant for laminar diffusion micromixers (Kamholz and Yager 2001).

In addition to a concentration distribution simulation, emission distribution simulations were created to incorporate the known discrepancies between concentration and emission information. Differences between these two models include optical thickness, as well as experiment specific error such as photobleaching and emission overlap (Coppeta and Rogers 1998), and are incorporated into the concentration simulation via MATLAB. The concentration and intensity profiles, and their respective mixing statistics, are shown in Fig. 6. Emission overlap is caused by fluorescent dyes exhibiting emissions within their non-targeted image. As most fluorescent dyes have long trailing ends perfect isolation of the emissions of the two dyes is not feasible, as a result Sulforhodamine G is visible in the reference image. This results in a damping effect within the ratiometric image, where the reference image imprints on the mixing profile over the reference profile. Emission overlap of the two dyes is determined by running a solution of one dye at a constant concentration through both channels and measuring

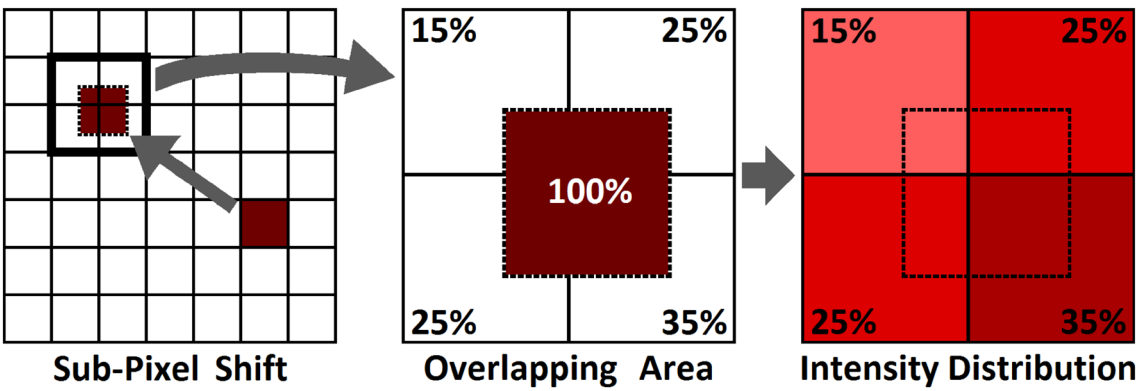

Fig. 5 Example of the subpixel accuracy ratiometric image correction using a sandpaper correction. For subpixel shifts, the intensity of the shifted pixel is distributed proportionally between overlapping regions

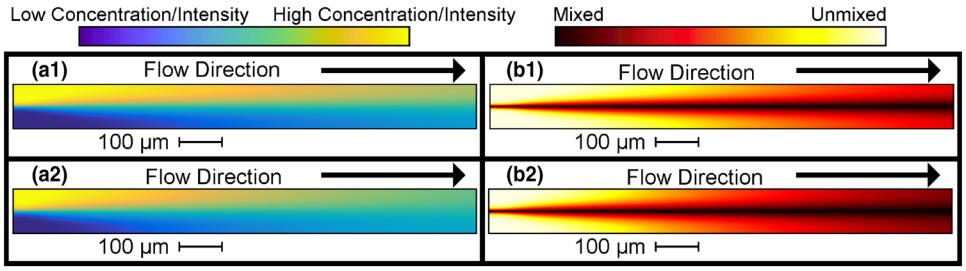

Fig. 6 **a1** Distribution of solute throughout a model microchannel with two inlets; one containing solute, and one containing pure water. **b1** The standard deviation for each vertical slice of the microchannel. **a2** The modeled intensity distribution, based on optical discrepancies (optical thickness, emission overlap, photobleaching) coupled with the solute distribution in **a1.** **b2** The standard deviation statistic for the intensity distribution as seen in **a2**

the emission of those dyes in both the mixing and reference images. The inclusion of emission overlap changes (Eq. 12) to:

$$R = \frac{\Phi_{1-1}\left[\varepsilon_1(\lambda_{\text{filt1}})C_1\dfrac{\left[1-\exp\left(-\{\varepsilon(\lambda_{\text{Ex}})C+\varepsilon_2(\lambda_{\text{filt1}})C_2\}L\right)\right]}{\varepsilon(\lambda_{\text{Ex}})C+\varepsilon_2(\lambda_{\text{filt1}})C_2}\right] + \Phi_{2-1}\left[\varepsilon_2(\lambda_{\text{filt1}})C_2\dfrac{\left[1-\exp\left(-\varepsilon(\lambda_{\text{Ex}})CL\right)\right]}{\varepsilon(\lambda_{\text{Ex}})C}\right]}{\Phi_{1-2}\left[\varepsilon_1(\lambda_{\text{filt2}})C_1\dfrac{\left[1-\exp\left(-\{\varepsilon(\lambda_{\text{Ex}})CL+\varepsilon_2(\lambda_{\text{filt1}})C_2\}L\right)\right]}{\varepsilon(\lambda_{\text{Ex}})C+\varepsilon_2(\lambda_{\text{filt1}})C_2}\right] + \Phi_{2-2}\left[\varepsilon_2(\lambda_{\text{filt2}})C_2\dfrac{\left[1-\exp\left(-\varepsilon(\lambda_{\text{Ex}})CL\right)\right]}{\varepsilon(\lambda_{\text{Ex}})C}\right]}, \tag{13}$$

where the subscripts 1 and 2 for the concentration C and the molar extinction coefficient ε represent properties of the mixing dye (Sulforhodamine G) and reference dye (Sulforhodamine 640), respectively. The subscripts for the Φ_{i-j} term represent the relative levels of fluorescence emission strength of dye i in capturing channel j (for example Φ_{1-2} represent the percentage of bleed of the mixing dye emission in the reference image). For further clarification, Φ_{i-j} does not represent the quantum efficiency.

Since the reference dye does not substantially bleed into the mixing image, the Φ_{2-1} term is removed and (Eq. 13) reduces to:

$$R = \frac{\Phi_{1-1}\left[\varepsilon_1(\lambda_{\text{filt1}})C_1\dfrac{\left[1-\exp\left(-\{\varepsilon(\lambda_{\text{Ex}})C+\varepsilon_2(\lambda_{\text{filt1}})C_2\}L\right)\right]}{\varepsilon(\lambda_{\text{Ex}})C+\varepsilon_2(\lambda_{\text{filt1}})C_2}\right]}{\Phi_{1-2}\left[\varepsilon_1(\lambda_{\text{filt2}})C_1\dfrac{\left[1-\exp\left(-\{\varepsilon(\lambda_{\text{Ex}})CL+\varepsilon_2(\lambda_{\text{filt1}})C_2\}L\right)\right]}{\varepsilon(\lambda_{\text{Ex}})C+\varepsilon_2(\lambda_{\text{filt1}})C_2}\right] + \Phi_{2-2}\left[\varepsilon_2(\lambda_{\text{filt2}})C_2\dfrac{\left[1-\exp\left(-\varepsilon(\lambda_{\text{Ex}})CL\right)\right]}{\varepsilon(\lambda_{\text{Ex}})C}\right]}. \tag{14}$$

Photobleaching is the reduction of a fluorophore's fluorescent emission due to relaxation caused by multiple

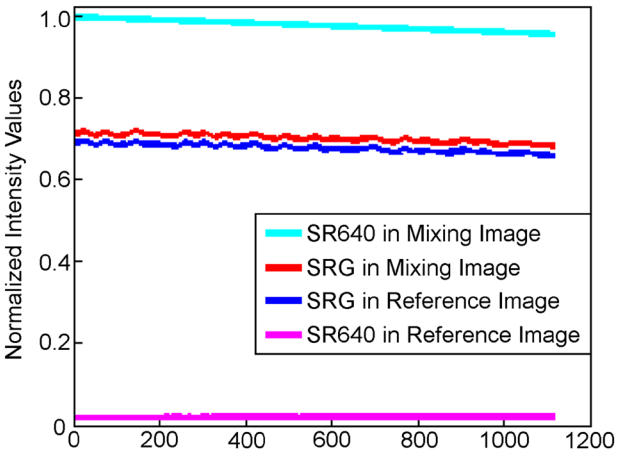

Fig. 7 Intensity of isolated Sulforhodamine G (SRG) and Sulforhodamine (SR640) emissions over the length of the channel, for both the mixing (low wavelength) and reference (high wavelength) images when excited with a 532 nm laser

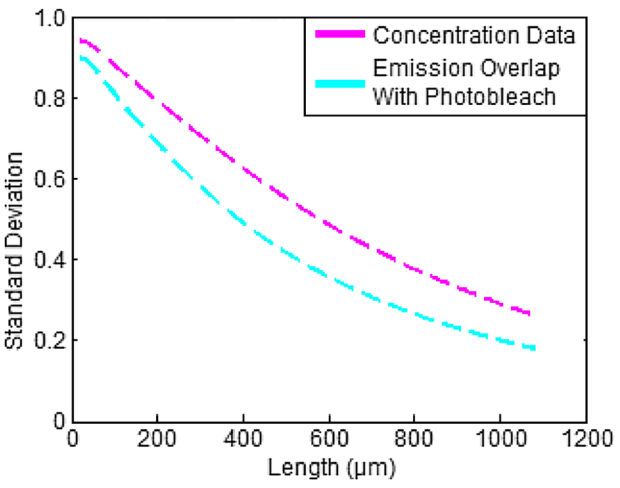

Fig. 8 Mixing statistics for the pure concentration distribution and intensity distributions, including optical thickness, reabsorption, emission overlap, and photobleaching

excitations (Song et al. 1995; Chen 2007). Rates for both the reference and mixing dyes were determined experimentally through the isolation and exposure of stationary dye slugs to the excitation source. Photobleaching can thus be imposed at each given location depending on the flow rate of the system. The amount of photobleaching at a given point in the microchannel for both dyes in both the mixing and reference images is shown in Fig. 7.

The mixing statistic over the length of a channel for the concentration distribution simulation and imaging simulation can be found in Fig. 8. These curves are used as calibration curves to be compared to the experimental results. Incorporation of optical thickness into the simulation shows a 24% increase in mixing over the length of the channel. This is primarily due to the transition from optically thick to optically thin as dye diffuses from regions of higher concentration to lower concentration. The incorporation of emission overlap and photobleaching into the simulation does not change the mixing statistic substantially, accounting for differences of less than 0.1%. The use of different fluorophores and filters could cause these effects to become significant in other instances.

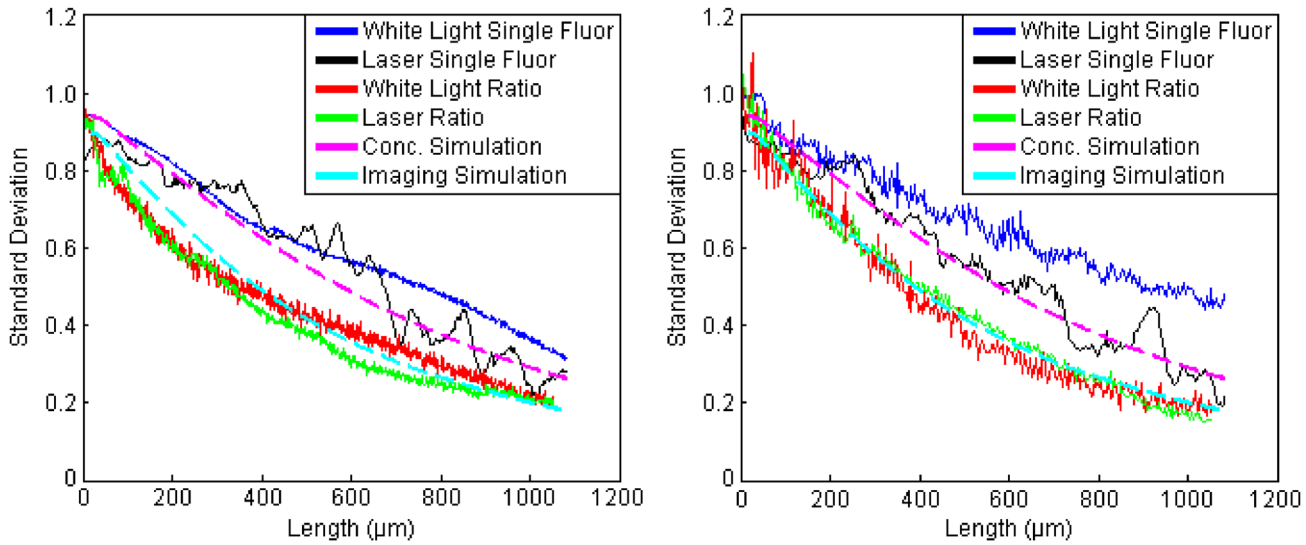

Fig. 9 (left) The standard deviation mixing statistic for both white light and laser illumination, and single dye and ratiometric imaging approaches using a CCD camera with a higher pixel density sensor (6.45×6.45-μm pixels). (right) The standard deviation mixing statistic for the same cases, using a CMOS camera with a low pixel density sensor (20×20-μm pixels). Both images contain the mixing statistic applied to both the concentration and imaging simulations

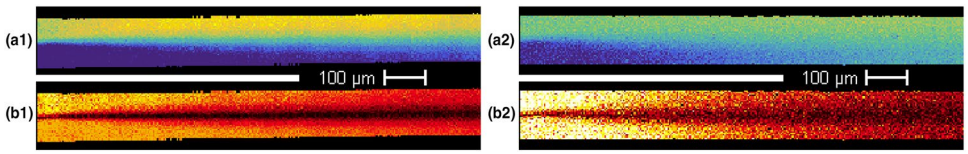

Fig. 10 **a** Intensity distribution for a laminar stream micromixer, recorded on a CCD (**a1**) or a CMOS (**a2**), using a single dye approach and excited using a white light source

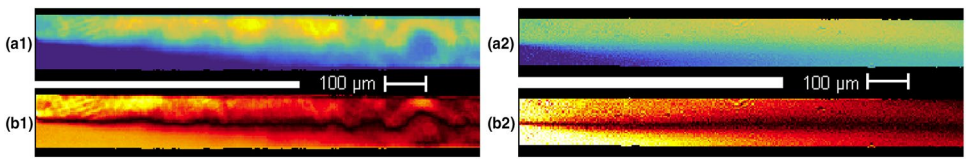

Fig. 11 **a** Intensity distribution for a laminar stream micromixer, recorded on a CCD (**a1**) or a CMOS (**a2**), using a single dye approach and excited using a white light source

Table 1 Standard deviation mixing statistic for various experiments conducted using a CCD camera compared to the raw data recorded as average percent difference for the given sets

Experiment	(A) (%)	(B) (%)	(C) (%)	(D) (%)
White light single	0.41	2.45	49.74	13.98
Laser light single	0.42	9.65	35.59	9.25
White light ratio	2.33	4.40	10.09	19.60
Laser light ratio	1.39	6.01	7.58	26.49

Fits: *(A)* lowpass filter, *(B)* exponential curve fit, *(C)* comparison to imaging simulation, *(D)* comparison to concentration simulation

Table 2 Standard deviation mixing statistic for various experiments conducted using a CMOS camera compared to the raw data recorded as average percent difference for the given sets

Experiment	(A) (%)	(B) (%)	(C) (%)	(D) (%)
White light single	2.05	2.85	70.21	28.91
Laser light single	1.42	8.13	31.78	7.43
White light ratio	5.17	7.30	6.73	24.61
Laser light ratio	2.10	3.81	5.60	22.38

Fits: *(A)* lowpass filter, *(B)* exponential curve fit, *(C)* comparison to imaging simulation, *(D)* comparison to concentration simulation

3.2 Laminar mixer: experimental

With the simulation to act as a comparative tool, experimental results for identical geometry were used to verify the accuracy of the technique. The quality of the sensor, the quality of the illumination source, as well as the inclusion of a reference dye were changed between experiments in order prove the techniques effectiveness under multiple conditions. Experiments were conducted for all combinations of these parameters. The mixing statistics for these experiments can be seen in Fig. 9, and their corresponding images can be seen in Figs. 10, 11, 12, 13.

Mixing cases were qualified in terms of four statistics: sensor noise, excitation bias, concentration model fit, and imaging model fit. Sensor noise is defined as the noise caused by the camera sensor converting intensity distributions into 12-bit levels within discretized pixels. This noise is high frequency and particularly prominent for CMOS sensors and ratiometric images. Sensor noise is quantified by running data through a custom lowpass filter (MATLAB) with a passband frequency of 0.01 Hz. To compensate for phase distortion, data were filtered forwards and backwards. The standard deviation of the filtered data set with respect to the raw data is used to quantify the sensor noise, where the larger values correspond to higher levels of noise within an image. The levels of high-frequency noise for all cases are shown Tables 1 and 2 for the CCD and CMOS, respectively.

Lower noise within a system corresponds with improved sensor quality, with reductions ranging from 51 to 87%. Single dye experiments for white light cases have less noise than their ratiometric counterparts due to the nature of ratiometric imaging. These images are constructed from two images both of which contain high-frequency noise, increasing the noise for these cases. This correlation does not carry over to laser illuminated cases, as excitation fluctuations exist for a range of frequencies. The higher frequency excitations are also filtered by the lowpass filter, leaving an increase in perceived noise over the sample for these cases.

Experiments were conducted at exposures that took advantage of the full range of bit values for the sensor, achieving the highest possible signal-to-noise ratio for a given case. The only time where the full range of the sensor could not be utilized were experiments that used the high-speed CMOS with a white light excitation source due to the high minimum frame rate in combination with the low intensity of dye emissions when excited with a white light. The resulting signal-to-noise ratio is much lower for the two affected cases.

Excitation error within the sample is determined by performing an exponential curve fit of the standard deviation for each case. The error is recorded as the percentage difference between these values and can be seen in Table 1. An exponential fit was selected as it matches the concentration and imaging simulations within a 1% error. Low frequency noise does not account for large gradients that exist over the whole image, like those caused by the inclusion of a white light source, but acts as an indicator for the effectiveness of the technique's ability to remove overlying patterns. Inclusion of the ratiometric technique reduced bias caused by laser excitation fluctuations by 38% for the CCD camera, and 53% for the CMOS camera. White light excitations are not

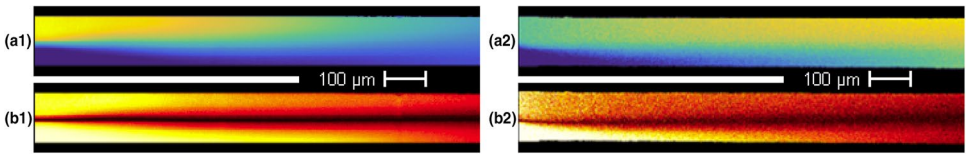

Fig. 12 **a** Intensity distribution for a laminar stream micromixer, recorded on a CCD (**a1**) or a CMOS (**a2**), using a single dye approach and excited using a white light source

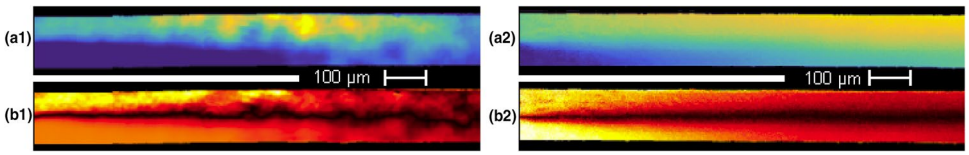

Fig. 13 **a** Intensity distribution for a laminar stream micromixer, recorded on a CCD (**a1**) or a CMOS (**a2**), using a single dye approach and excited using a white light source

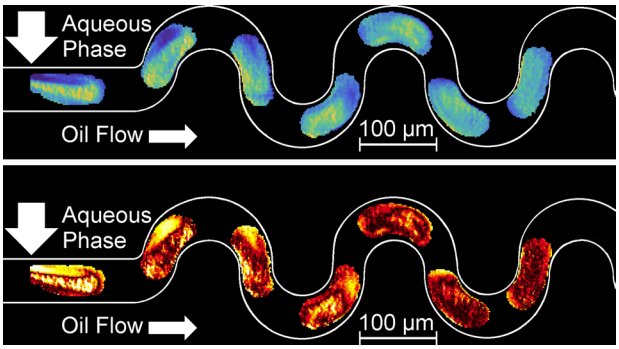

Fig. 14 Pseudocolored ratio distribution (above) and mixing value distribution (below). Measurements are taken for continuous fluid volumes

Table 3 The best fit diffusion coefficients for each experiment, the difference (recorded as a percentage difference between each experiment and the best fit model selected), and the difference between each fit and our imaging simulation fit (Tables 1/2)

Experiment	Camera	Diffusion coeff. (cm^2/s)	Error of fit (%)	Difference of fit and simulation
Laser light ratio	Coolsnap	2.7 e − 06	6.67	0.2 e − 06
	FastCam	2.5 e − 06	5.60	0.0 e − 06
White light ratio	Coolsnap	2.2 e − 06	6.70	0.3 e − 06
	FastCam	2.7 e − 06	6.29	0.2 e − 06
Laser light single	Coolsnap	1.8 e − 06	10.65	0.7 e − 06
	FastCam	1.8 e − 06	9.20	0.7 e − 06
White light single	Coolsnap	1.2 e − 06	3.64	1.3 e − 06
	FastCam	0.9 e − 06	4.21	1.6 e − 06

prone to these kinds of fluctuations, so a ratiometric image does not help in the reduction of noise for these cases.

Systematic imaging error between samples is calculated by comparing the standard deviation of a set to the constructed COMSOL simulation. Since there are systematic errors unique to ratiometric imaging, single dye experiments are compared to cases that consider optical thickness and photobleaching of the mixing dye, while ratiometric images are compared to cases that consider optical thickness, emission overlap, and photobleaching for both dyes. The comparison between the experimental mixing statistics and both the concentration and imaging distributions can be seen in Table 1 for the CCD and Table 2 for the CMOS.

For all cases, the ratiometric image improves the effectiveness of the mixing technique in matching the expected fluorescent output by values ranging from 16 to 59%. These large intensity gradients can be seen in Fig. 12a where the high fluorescent output stream decreases significantly over the length of the channel. These data follow the mixing profile determined from the COMSOL simulation closely, with an error of only 13.98%, but it can be seen that the concentration profile is significantly different than the expected profile in Fig. 6a1. This can be explained by looking at the change in intensity at different points throughout the channel. Due to the sample being optically thick, the average intensity of each cross-section should increases as the dye diffuses.

The effect of large intensity gradients in skewing mixing statistics becomes apparent when comparing fluorescent output to the concentration distribution profile. In these cases the imaging effects and the excitation gradients work in opposition to one another, lowering and raising the perceived mixing for all cross-sections. As a result the single dye cases more closely align with the concentration simulation over the imaging simulation for all cases, as shown when comparing the error in Table 1 to the error in Table 1. It should be noted that this is not the removal of systematic error from the sample, but rather the inclusion of an additional system specific error that works in opposition to the initial errors. This is illustrated by looking at the lowest error case; laser excitation, single dye, recorded using a CMOS camera, shows that this data set and the concentration model only deviate from one another by 7.43%. Inspection of the images comprising this data set, Fig. 11a1, b1, shows that these images are not following the expected mixing profile shown in Fig. 6. Specifically, the standard deviation profile should show the region of highest mixing should be the central pixel of every cross section, and the degree of mixing should decrease evenly as one looks toward the edges of the channel. The mixing seen in Fig. 6b1 lacks this symmetry and shows high degrees of mixing at both the centerline and the channel edges, whereas the ratiometric image statistic in Fig. 11b2 exhibits a similar behavior.

In addition to comparing experimental data to concentration and imaging simulations, these simulations were used to determine the diffusion coefficient that most accurately reflects the behavior of the mixing curves in Fig. 9. Diffusion coefficients were iterated in COMSOL from 0.6×10^{-10} to 4.0×10^{-10} m^2s^{-1} by steps of 0.1×10^{-10} m^2s^{-1}. For the ratiometric imaging cases the effects of optical thickness, photobleaching, and optical bleed are incorporated into the simulation, while the single dye simulations only consider optical thickness and photobleaching. The different cases and their related diffusion coefficients can be found in Table 3. These best fit simulations were compared to the experimental data in the error of fit column, and the difference between the best fit simulation and the simulation using the actual diffusion coefficient is recorded in the difference of fit and simulation column. Given that the diffusion coefficient from the literature is given as 2.5×10^{-10} m^2s^{-1} (Jia et al. 2012), it can be seen that the ratiometric imaging technique is far more accurate than that of the single dye approach.

3.3 Droplet mixer: characterization

Mixing statistics were also calculated for droplet systems using a laser as an excitation source. Droplet micromixers take advantage of chaotic advection, reordering and redistribution fluid within the sample. The high speed of the droplet works in combination with wall effects to result in recirculation throughout the sample, as predicted in (Ismagilov et al. 2004; Tice et al. 2004; Stone and Stone 2005). Droplets are formed from an aqueous dye solution, using a three-pronged injector, consisting of one inlet with both mixing and reference dye, surrounded by two reference dye inlets, a total of three co-flowing streams. These streams flow a short distance to a T-junction geometry which pinches off the droplets with an immiscible continuous phase. The continuous phase used is Perfluorodecalin (PFD) 95% (Sigma Aldrich), which provides a lubricating film between the surface of the microchannel and the droplet, as well as acting as buffer between droplets within the microchannel. Velocity and size of these droplets are controlled by the velocity of the continuous phase (Tan et al. 2005; Guo et al. 2011; Tirandazi and Hidrovo 2016). Mixing is enhanced in this system by alternating the rate of shear stress across the droplet as it travels down the serpentine (Stone and Stone 2005).

Increasing the speed at which the droplets travel through the micromixer increases the shear force on the surface of the droplet, promoting recirculation and mixing. This increase in recirculation comes at the cost of decreasing the time that the dye within the droplet has to diffuse. Since these forces work in opposition, a correlation between droplet speed and level of mixing cannot be inferred upon simple inspection of the system. To determine this relationship, droplet mixing

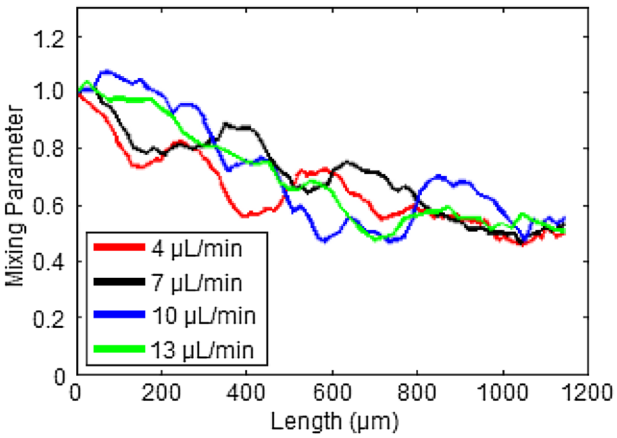

Fig. 15 Mixing parameter of the mid-plane for the droplet sample using oil flow rates of 4, 7, 10, and 13 μL/min and dye flow rate of 4 μL/min

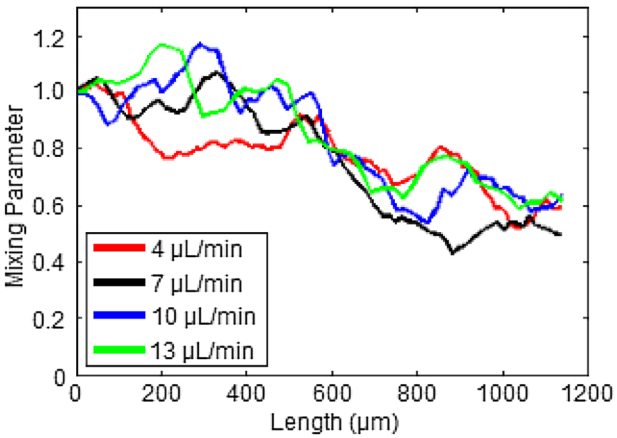

Fig. 16 Mixing parameter of the bottom plane for the droplet sample using oil flow rates of 4, 7, 10, and 13 μL/min and dye flow rate of 4 μL/min

over the length of the channel was determined for PFD flow rates of 4 μL/min, 7 μL/min, 10 μL/min, and 13 μL/min.

Where laminar stream micromixers are characterized using a single image of a channel and comparing statistics for successive rows of pixels down the length of the channel, droplet micromixers take mixing statistics over time, using multiple images of the same droplet as it travels through the channel. Visualization of these droplets requires the use of the CMOS camera, which was operated at 10,000 frames per second. Data were collected using ratiometric imaging and a laser excitation source exclusively, as a reference dye was necessary to track the mixing fluids and white light illumination is far too weak to cause significant dye phosphorescence.

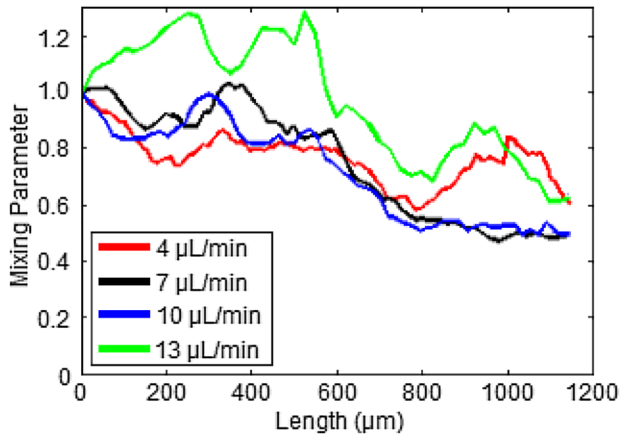

Fig. 17 Mixing parameter of the top plane for the droplet sample using oil flow rates of 4, 7, 10, and 13 μL/min and dye flow rate of 4 μL/min

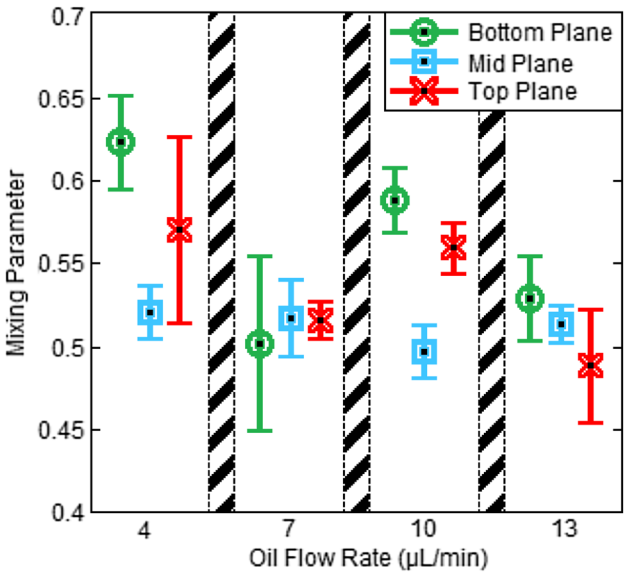

Fig. 18 End value mixing parameter for all 4 flowrates and 3 planes. Experiments were conducted 15 times for each set of parameters

Due to the injection geometry within the sample, the co-flowing streams exhibit some level of diffusing before entering the main channel. In the laminar diffusion mixer the two mixing fluids do not come in contact before meeting at the Y-junction and axial diffusion is negligible, so it can be assumed that fluid at the vertex of the micromixer is completely unmixed, and thus for the laminar stream cases $\sigma_o \approx 1$. To account for the pre-mixing behavior in the droplet system the mixing parameter was normalized to the form:

$$\eta = \frac{\frac{\sigma_T}{\mu}}{\frac{\sigma_o}{\mu}}. \quad (15)$$

Experiments were conducted at for oil flow rates of 4 μL/min, 7 μL/min, 10 μL/min, and 13 μL/min with a total dye flow rate of 8 μL/min for all cases. Mixing information was taken for a 5 μm thick focal depth taken at the mid-plane of the sample, as well as focal planes centered 10 μm from both the top and bottom of the channel. The intensity distributions taken at the mid-plane using a flow rate of 10 μL/min is shown in Fig. 14. The results of these experiments for the mid-plane can be found in Fig. 15, and for the bottom and top planes in Figs. 16 and 17, respectively. Statistics collected for these droplet micromixers have large fluctuations in their profiles, whereas an ideal diffusion profile would decay to zero. This effect can be largely attributed to out-of-plane mixing (Stone and Stone 2005). Since droplets moving through a microchannel exhibit internal recirculation, there is a movement of dye throughout the observed focal plane at all points in time. This can be corrected through utilization of a microscope objective with a depth of view equal to that of the thickness of the channel. Unfortunately objectives with such large focal depths also have low magnifications, making them unsuited for data collection at the microscale (Fig. 18).

These fluctuations are particularly prominent for the top and bottom plane measurements which can be attributed to the nature of recirculation patterns. For these recirculation zones the bulk of the droplet volume recirculates from the surface of the droplet to the center of the droplet (Baroud et al. 2010). When the focal plane is set at the center of the droplet, there is less internal advection between frames, resulting in smaller fluctuations in statistics over time. As the droplet mixes more completely, the out-of-plane effects become smaller, but these effects can still be seen in the up to an 8% difference in mixing values for the 4 μL/min case, shown in Fig. 18.

The results taken from the mid-plane in Fig. 15 show a non-correlation between the level of mixing and the speed at which the droplet travels through the micromixer. Mid-plane results in Fig. 18 show all four flow rates show droplets becoming $51 \pm 2\%$ mixed upon traveling 1100 μm (through two full serpentine motions). These results were verified for 15 droplets for each case and these mixing values and the error within 99%. End value mixing values were gathered by averaging the last 10% of recorded values to reduce fluctuations from out-of-plane effects.

4 Conclusion

A two-dye ratiometric imaging technique was compared to a single-dye imaging technique for determining the homogeneity of a microfluidic mixing case. The purpose of this ratiometric technique is to remove excitation information while retaining concentration information in the fluorescent

emission. Sulforhodamine G and Sulforhodamine 640 were used as the mixing and reference indicator, respectively. Excitation was provided from two sources, either a low intensity white light source exhibiting a more even intensity profile, or a higher power continuous wave laser that displayed substantial spatial intensity fluctuations. The emissions of these two dyes are separated using a dichroic mirror and recorded using a 12-bit digital camera; either a more accurate CCD or a faster CMOS. Sandpaper images were used to form cross-correlations between the two images, allowing for proper alignment between pixels and their physical locations. Homogeneity for both singular and ratiometric images is determined by taking the standard deviation of the recorded scalar values across the sample.

The imaging technique was characterized using a laminar stream diffusion micromixer. This laminar stream mixer was simulated in COMSOL Multiphysics and imaging effects were incorporated into these simulations using MATLAB. These simulations were compared to experimental results captured using two excitation sources, two different camera sensors, and either a single-dye or ratiometric approach. Experimental results were characterized in terms of the levels of low and high-frequency noise throughout a sample, and compared to the simulated results. Results show that ratiometric images can eliminate excitation information and match the imaging simulation within 14% and 17% for both a CCD and a CMOS sensor as opposed to the single-dye approach which exhibit accuracy of 32% and 36%, respectively. Even the "uniform" white light excitation sources have large gradients over the length of the microchannel which can be corrected through the use of a ratio. The nonlinear relationship between dye emissions and dye concentration as well as the inclusion of ratiometric imaging both lower the calculated statistic for a given cross section, but these effects are easy to quantify and accurate mixing information can be inferred from a given mixing statistic.

This technique was further used to characterize a droplet micromixer, which uses internal advection to shorten diffusion lengths thus increasing the rate of diffusion. Due to the complex physics of these systems, they are difficult to both model and simulate, making them suitable for experimental analysis. The droplet micromixer was characterized for a variety of continuous phase flow rates, controlling the size of the droplets and the rate at which they pass through the serpentine channel. Increasing the oil flow rate increases recirculation within the droplet while shortening the time dye has to diffuse within the system. Droplets were analyzed at three different focal planes to better understand the mixing behavior occurring throughout the whole droplet. It was found that varying the continuous phase flow rate in our system had a negligible effect on the rate of mixing throughout the sample, as droplets became $51 \pm 2\%$ mixed over time. Out-of-plane measurements still show the same mixing trends, but contain larger fluctuations over time due to the bulk movement of fluid through the sample. With our mixing diagnostic verified and shown to work in complex mixing systems, we believe it is possible to implement this in a variety of micromixers for the purpose of optimization and increasing the mixing efficiency.

Acknowledgements This work was supported by The Northeastern University start-up funds, and a NSF Award Grant CBET-1522841.

References

Abbas Y, Miwa J, Zengerle R, Stetten F, Von (2013) Active continuous-flow micromixer using an external braille pin actuator array. Micromachines 4:80–89. https://doi.org/10.3390/mi4010080

Baker M (2012) Digital PCR hits its stride. Nat Methods 9:541–544. https://doi.org/10.1038/nmeth.2027

Baroud CN (2010) Dynamics of microfluidic droplets. Lab Chip 10:2032–2045. https://doi.org/10.1039/c001191f

Baroud CN, Gallaire F, Dangla R (2010) Dynamics of microfluidic droplets. Lab Chip 10:2032–2045. https://doi.org/10.1039/c001191f

Carroll B, Hidrovo C (2012) Droplet collision mixing diagnostics using single fluorophore LIF. Exp Fluids 53:1301–1316. https://doi.org/10.1007/s00348-012-1361-x

Chen J (2007) Photobleaching correction in fluorescence microscopy images. J Phys Conf Ser 16:1–8. https://doi.org/10.1088/1742-6596/90/1/012068

Christensen KT, Natrajan VK (2010) Non-intrusive measurements of convective heat transfer in smooth- and rough-wall microchannels: laminar flow. Exp Fluids 49:1021–1037. https://doi.org/10.1007/s00348-010-0845-9

Coppeta J, Rogers C (1998) Dual emission laser induced fluorescence for direct planar scalar behavior measurements. Exp Fluids 25:1–15

Dittrich PS, Manz A (2006) Lab-on-a-chip: microfluidics in drug discovery. Nature 5:210–218. https://doi.org/10.1038/nrd1985

Gashti MP, Asselin J, Barbeau J et al (2016) A microfluidic platform with pH imaging for chemical and hydrodynamic stimulation of intact oral biofilms. Lab Chip 16:1412–1419. https://doi.org/10.1039/C5LC01540E

Guo Z, Zeng Q, Zhang M et al (2011) Sensors and actuators a: physical valve-based microfluidic droplet micromixer and mercury (II) ion detection. Sens Actuators 172:546–551. https://doi.org/10.1016/j.sna.2011.09.019

Hardy BS, Uechi K, Zhen J, Kavehpour HP (2009) The deformation of flexible PDMS microchannels under a pressure driven flow. Lab Chip 9:935–938. https://doi.org/10.1039/b813061b

Hassan A (1984) Stirring by chaotic advection. J Fluid Mech 143:1–21

Hidrovo CH, Hart DP (2001) Emission reabsorption laser induced fluorescence (ERLIF) film thickness measurement. Meas Sci Technol 12:467–477. https://doi.org/10.1088/0957-0233/12/4/310

Huebner A, Srisa-art M, Holt D et al (2007) Quantitative detection of protein expression in single cells using droplet microfluidics. Chem Commun 2:1218–1220. https://doi.org/10.1039/b618570c

Huebner A, Bratton D, Whyte G et al (2009) Static microdroplet arrays: a microfluidic device for droplet trapping, incubation and release for enzymatic and cell-based assays. Lab Chip 9:692–698. https://doi.org/10.1039/b813709a

Ismagilov F, Tice J, Song H et al (2004) Microfluidic systems for chemical kinetics that rely on chaotic mixing in droplets. Philos Trans R Soc 362:1087–1104

Jia P, Yang Q, Gong Y, Zhao J (2012) Dynamic exchange of counterions of polystyrene sulfonate. J Chem Phys 136:1–7. https://doi.org/10.1063/1.3688082

Jones S, Thomas O, Aref H (1989) Chaotic advection by laminar flow in a twisted pipe. J Fluid Mech 209:335–357

Kamholz AE, Yager P (2001) Theoretical analysis of molecular diffusion in pressure-driven laminar flow in microfluidic channels. Biophys J 80:155–160. https://doi.org/10.1016/S0006-3495(01)76003-1

Kim M, Yoda M (2010) Dual-tracer fluorescence thermometry measurements in a heated channel. Exp Fluids 49:257–266. https://doi.org/10.1007/s00348-010-0853-9

Kim TJ, Kim M, Hann S et al (2015) Thermal characterization of microheated microchannels with spatially resolved two-color fluorescence thermometry. Microelectromechanical Syst 24:115–125

Kise DP, Magana D, Reddish MJ, Dyer RB (2014) Lab on a chip hyperspectral imaging detection. Lab Chip 14:584–591. https://doi.org/10.1039/c3lc51171e

Kling K, Mewes D (2003) Quantitative measurements of micro- and macromixing in a stirred vessel using planar laser-induced fluorescence. J Vis 6:165–173. https://doi.org/10.1007/BF03181621

Kling K, Mewes D (2004) Two-colour laser induced fluorescence for the quantification of micro- and macromixing in stirred vessels. Chem Eng Sci 59:1523–1528. https://doi.org/10.1016/j.ces.2004.01.015

Lin F, Saadi W, Rhee W, Wang S (2004) Generation of dynamic temporal and spatial concentration gradients using microfluidic devices. Lab Chip 164–167

Liu RH, Stremler M, Sharp KV et al (2000) Passive mixing in a three-dimensional serpentine microchannel. J Microelectromechanical Syst 9:190–197. https://doi.org/10.1109/84.846699

Mayinger F, Bockhorn H, Mewes D et al (2010) Micro and macro mixing. Scientific Publishing Services, Berlin

Natrajan VK, Christensen KT (2009) Two-color laser-induced fluorescent thermometry for microfluidic systems. Meas Sci Technol. https://doi.org/10.1088/0957-0233/20/1/015401

Pav J, Jana Ž, Milavec M (2016) Assessment of the real-time PCR and different digital PCR platforms for DNA quantification. Anal Bioanal Chem 408:107–121. https://doi.org/10.1007/s00216-015-9107-2

Sakakibara J, Adrian RJ (1999) Whole field measurement of temperature in water using two-color laser induced fluorescence. Exp Fluids 26:7–15

Sakakibara J, Adrian RJ (2004) Measurement of temperature field of a Rayleigh-Benard using two-color laser-induced fluorescence. Exp Fluids 37:331–340. https://doi.org/10.1007/s00348-004-0821-3

Schwille P (2005) Characterization of the photoconversion on reaction of the fluorescent protein Kaede on the single-molecule level. Biophys J 89:3446–3455. https://doi.org/10.1529/biophysj.105.061713

Shi X, Xiang Y, Wen L, Chen J (2012) CFD analysis of flow patterns and micromixing efficiency in a Y–type microchannel reactor. Am Chem Soc 51:13944–13952. https://doi.org/10.1021/ie300985q

Soloff SM, Al E (1997) Distortion compensation for generalized stereoscopic particle image velocimetry distortion compensation for generalized stereoscopic particle image velocimetry. Meas Sci Technol 8:1441

Song L, Hennink EJ, Young T, Tanke HJ (1995) Photobleaching kinetics of fluorescein in quantitative fluorescence microscopy. Biophys J 68:2588–2600

Stone ZB, Stone HA (2005) Imaging and quantifying mixing in a model droplet micromixer. Phys Fluids 17:1–11. https://doi.org/10.1063/1.1929547

Tan Y, Cristini V, Lee AP (2005) Monodispersed microfluidic droplet generation by shear focusing microfluidic device. Sens Actuators B 114:350–356. https://doi.org/10.1016/j.snb.2005.06.008

Tice JD, Lyon AD, Ismagilov RF (2004) Effects of viscosity on droplet formation and mixing in microfluidic channels. Anal Chim Acta 507:73–77. https://doi.org/10.1016/j.aca.2003.11.024

Tirandazi P, Hidrovo CH (2016) Generation of uniform liquid droplets in a microfluidic chip using a high-speed gaseous microflow. In: ASME 2016 14th international conference on nanochannels, microchannels, and minichannels, pp 1–6. https://doi.org/10.1115/ICNMM2016-8061

Tirandazi P, Hidrovo CH (2017) Liquid-in-gas droplet microfluidics; experimental characterization of droplet morphology, generation frequency, and monodispersity in a flow-focusing microfluidic device. J Micromech Microeng 27:075020

Waggoner A (2006) Fluorescent labels for proteomics and genomics. Curr Opin Chem Biol 10:62–66. https://doi.org/10.1016/j.cbpa.2006.01.005

Wang NS, Rinaudo P, McAvoy T (1988) Laser-induced fluorescnece monitoring of multicomponent aromatic amino acids. 196th Natl ACS Meet

Wang MM, Tu E, Raymond DE et al (2005) Microfluidic sorting of mammalian cells by optical force switching. Nature Biotechnology 23:83–87. https://doi.org/10.1038/nbt1050

Wu Z, Nguyen N (2005) Rapid mixing using two-phase hydraulic focusing in microchannels. Biomed Microdevices 7:13–20

Yamada M, Kasim V, Nakashima M et al (2004) Continuous cell partitioning using an aqueous two-phase flow system in microfluidic devices. Biotechnol Bioeng 88:. https://doi.org/10.1002/bit.20276

Yang Z, Matsumoto S, Goto H et al (2001) Ultrasonic micromixer for microfluidic systems. Sens Actuators 93:266–272